Research Article

Journal of Environmental Nanotechnology

Comparative Green and Wet-chemical Synthesis of ZnO Nanoparticles: Enhanced Photocatalytic and SERS Performance of Defect-rich Nanostructures

Dipti N. Kashyap[1], N. Shalom[2], S. Mayakannan[3,4*], M. Muthuraj[5], A. Thanikasalam[6] and Abdussalam Ali Ahmed[7]

[1]Department of Mechanical Engineering, Yeshwantrao Chavan College of Engineering, Wanadongri, Hingna Road, Nagpur, MH, India
[2]Department of Mechanical Engineering, Karpagam College of Engineering, Coimbatore, TN, India
[3]Department of Mechanical Engineering, Rathinam Technical Campus, Coimbatore, TN, India
[4]Department of Mechanical Engineering, Saveetha School of Engineering, Saveetha Institute of Medical and Technical Sciences, SIMATS, Chennai, TN, India
[5]Department of Mechanical Engineering, NPR College of Engineering and Technology, Dindigul, TN, India
[6]Department of Marine Engineering, Academy of Maritime Education and Training (AMET) Deemed to University, Kanathur, Chennai, TN, India
[7]Mechanical and Industrial Engineering, Faculty of Engineering, Bani Waleed University, Bani Walid, LY, North Africa
Received: 11.04.2026 Accepted: 06.05.2026 Published: 30.06.2026
*kannanarchieves@gmail.com

ABSTRACT

Zinc oxide nanoparticles were synthesized using both a conventional wet-chemical method and eco-friendly green synthesis routes employing plant extracts from *Moringa oleifera*, *Terminalia chebula*, and *Aloe vera*. The study provides a comparative evaluation of these synthesis approaches to identify environmentally sustainable methods capable of producing high-performance ZnO nanomaterials. Thermogravimetric analysis was used to determine suitable calcination temperatures (400–700 °C), and the structural, morphological, and optical properties of the synthesized nanoparticles were characterized using XRD, SEM–EDS, DLS, UV–Vis, ATR–FTIR, Raman spectroscopy, and SAED. XRD results confirmed the formation of hexagonal wurtzite ZnO with crystallite sizes ranging from 11.1 to 72.2 nm. UV–Vis analysis indicated bandgap energies ranging from 3.11 to 4.22 eV, demonstrating size-dependent quantum confinement effects. Photocatalytic studies under 365 nm UV irradiation showed that *Moringa oleifera*–mediated ZnO nanoparticles achieved the highest methyl orange degradation efficiency of 67% within 180 min, outperforming nanoparticles synthesized using *Aloe vera* (60%), *Terminalia chebula* (35%), and the wet-chemical method (61% and 32% at different calcination temperatures). Surface-enhanced Raman scattering (SERS) analysis of *L*-phenylalanine demonstrated an enhancement factor on the order of 10^2, attributed to defect-mediated charge-transfer interactions. The results demonstrate that green-synthesized ZnO nanoparticles exhibit improved photocatalytic performance and sensing capabilities, highlighting their potential as multifunctional materials for environmental remediation, sensing applications, and bioactive components in bone regeneration systems.

Keywords: Photocatalysis; *Terminalia chebula*; Methyl orange; Green synthesis; Raman spectroscopy.

1. INTRODUCTION

In recent decades, zinc oxide nanoparticles (ZnONPs) have garnered significant interest owing to their distinctive physical properties, which encompass high chemical stability and sensitivity, advantageous mechanical properties, optical attributes, and electrical conductivity that varies with atmospheric conditions (in both oxidizing and reducing environments). Neem-flower-mediated ZnONPs showed good stability, strong antioxidant and antimicrobial activity, and minimal toxicity to normal cells. These eco-friendly nanoparticles are promising for therapeutic and bioengineering uses (Mohanasundaram and Mary, 2025). Several studies have reported that plant-mediated ZnO nanoparticles exhibit enhanced antibacterial, antioxidant, and anticancer properties with improved biocompatibility (Mohammadzadeh *et al.* 2024; Jothinathan and Suseem, 2026). Advanced nanomaterials synthesized by green and bio-assisted approaches have gained significant attention for biomedical, environmental, and catalytic applications due to their enhanced functionality, reduced toxicity, and sustainable fabrication routes. Among them, ZnO-based nanostructures have demonstrated remarkable multifunctionality. PEG–beta-carotene–curcumin–zinc oxide (PEG–Beta–Cur–ZnO) nanoparticles exhibited superior stability along with enhanced larvicidal, antibacterial, and anticancer performance compared to their individual constituents (Suresh *et al.* 2026). Similarly, plant gum-mediated ZnONPs derived from *Prosopis juliflora* showed strong antimicrobial, antioxidant, antidiabetic, and anti-inflammatory activities with good biocompatibility (Thanjavur *et al.* 2025). Doping and hybridization strategies further

improve ZnO performance; Cu-doped ZnONPs displayed enhanced antibacterial, antifungal, antioxidant, and anticancer efficacy (Kothandaraman *et al.* 2025), while ZnO/Fe_3O_4 nanocomposites demonstrated reduced cell viability in HCT116 cancer cells and strong antibacterial action against Gram-negative strains (Almoneef *et al.* 2025).

Ag/ZnO nanocomposites exhibited excellent photocatalytic dye degradation and notable antibacterial activity (Chhetri *et al.* 2025). Similarly, biogenic Ag nanoparticles showed strong antibacterial and antioxidant properties with minimal toxicity in zebrafish embryo models (Mahendran *et al.* 2025; Tharani *et al.* 2023). CeO_2 nanoparticles synthesized using *Moringa oleifera* extract demonstrated reduced bandgap energy and strong antimicrobial performance (Jayabal, 2025), while Bi_2O_3 nanoparticle-embedded polymer films exhibited high antimicrobial efficiency with acceptable cytocompatibility for biomedical coatings (Hasanin *et al.* 2025). Particularly, *Terminalia chebula*, a medicinal plant rich in phenolics and bioactive compounds, has been widely used as a reducing and stabilizing agent for nanoparticle synthesis. Extract-mediated Ag, Ni, and NiO nanoparticles have shown promising antibacterial, antioxidant, anticancer, and catalytic dye degradation performance (Kumar *et al.* 2025; Moulana *et al.* 2023; Kareem and Vijaya Lakshmi, 2022). Ethanolic extracts of *T. chebula* demonstrated high radical-scavenging activity and significant enzymatic antioxidant content (Elsadek and Al-Numair, 2024), while fermented extracts improved carbonation and durability in lime-based heritage materials (Wani and Thirumalini, 2024), indicating the plant's versatile functional chemistry.

Beyond single-metal systems, multi-metallic and noble metal nanoparticles synthesized by plant extracts have also exhibited enhanced therapeutic efficiency. *Aloe vera*–mediated ruthenium nanoparticles showed selective anticancer activity with minimal toxicity to healthy cells (Begum *et al.* 2025), and ZnO nanostructures synthesized using *Aloe vera* extract demonstrated improved morphology and functional performance (Ibupoto *et al.* 2024). Furthermore, nano-enabled formulations such as nano-emulsion gels have demonstrated enhanced skin regeneration and burn healing efficacy (Miastkowska *et al.* 2020), highlighting the translational potential of nanotechnology in advanced therapeutic systems (Kyana *et al.* 2025).

Despite extensive studies on ZnO nanoparticles synthesized through either conventional chemical or green routes, a systematic comparison of their structural, optical, photocatalytic, and sensing performances remains limited. In particular, the influence of different plant-mediated green synthesis routes on multifunctional ZnO nanoparticle properties has not been clearly established. Therefore, this study aims to comparatively investigate ZnO nanoparticles synthesized via a conventional wet-chemical method and green synthesis using *Moringa oleifera*, *Terminalia chebula*, and *Aloe vera* extracts. The novelty of this work lies in identifying the most effective eco-friendly synthesis route for producing multifunctional ZnONPs with enhanced photocatalytic and SERS sensing performance suitable for environmental and biomedical applications.

2. MATERIALS AND METHODS

2.1 Materials

Extracts were derived from the leaves of *Moringa oleifera* (Moringaceae), the fruits of *Terminalia chebula* (Combretaceae), and *Aloe vera* gel (Asphodelaceae). Zinc nitrate hexahydrate ($Zn(NO_3)_2{\cdot}6H_2O$) served as a zinc precursor for synthesizing zinc oxide nanoparticles (ZnONPs). Ammonia solution (NH_4OH) was used to regulate the pH during nanoparticle synthesis. Methyl orange (MO) and *L*-phenylalanine (*L*-Phe) served as model compounds for photocatalytic degradation and adsorption/SERS investigations, respectively.

2.2 Synthesis of ZnO

2.2.1 Wet Chemical Synthesis

The ultrasonic cleaner was employed, and 25 g of zinc nitrate hexahydrate ($Zn(NO_3)_2{\cdot}6H_2O$) was dissolved in 30 mL of deionized water, yielding a clear and homogeneous precursor solution. The solution was agitated incessantly for 10 min at 25 °C (Thanikodi and Jothi, 2026). An aqueous ammonia solution (1:1, v/v) was subsequently added dropwise while maintaining continual stirring until the pH reached around 9–10, thereby promoting the formation of zinc hydroxide intermediates. Subsequent pH adjustment was performed using a 2 M ammonia solution to guarantee full precipitation. The resultant precipitate was isolated using filtering, meticulously rinsed with distilled water to remove residual contaminants, and dried at 120 °C for 12 h (Errico *et al.* 2015). The dried product underwent heat treatment at 180 °C for 1 h to yield ZnO nanoparticles.

2.2.2 Green Synthesis

The green synthesis methodology used extracts from *Moringa oleifera* leaves, *Terminalia chebula* fruits, and *Aloe vera* gel.

Aloe vera extract: Fresh *A. vera* peels were meticulously cleansed, diced, and combined with pure water in a 1:10 (w/v) ratio. The mixture was heated to 50 °C for 1 h to enhance the extraction of bioactive chemicals, subsequently cooled to ambient temperature, and filtered to get a clear extract. Then, 5 mL of the produced *A. vera* extract was incorporated into a 10 mM solution of zinc nitrate hexahydrate ($Zn(NO_3)_2{\cdot}6H_2O$) and continuously stirred at 100 °C for 1.5 h. The

emergence of a precipitate signified nanoparticle production. The resultant product was filtered, repeatedly rinsed by deionized water to eliminate residual contaminants, and air-dried to yield *Aloe vera*–mediated ZnO nanoparticles (Ahmadi *et al.* 2022).

Terminalia chebula fruit extract: Fresh *T. chebula* fruits were cleansed, pulverized, and the resultant juice was strained. One mL of the filtrate was diluted to 50 mL with distilled water and subsequently filtered to eliminate insoluble residues. Then, 5 mL of the resulting extract was incorporated into 20 mL of 0.1 M aqueous $Zn(NO_3)_2 \cdot 6H_2O$ solution while maintaining continuous stirring at ambient temperature. The emergence of a precipitate signified the commencement of ZnO nanoparticle production. The resultant product was obtained by centrifugation, subjected to multiple washes with deionized water to eliminate unreacted species, and subsequently dried at ambient temperature to yield *Terminalia chebula*–mediated ZnO nanoparticles (Lavanya *et al.* 2023).

Moringa oleifera extract: 8 g of the finely powdered dried *M. oleifera* leaves was combined with 450 mL of deionized water, and the combination was permitted to remain at ambient temperature for 48 h to promote the extraction of bioactive phytochemicals, and thereafter underwent filtration to yield a clear extract. Subsequently, 4 g of $Zn(NO_3)_2 \cdot 6H_2O$ were dissolved in 400 mL of the produced leaf extract while maintaining continuous agitation. After 10 minutes, the emergence of a precipitate signified the synthesis of ZnO precursor particles (Devi, 2026). The products were subsequently filtered, thoroughly washed by distilled water, and air-dried to yield *Moringa oleifera*–mediated ZnO nanoparticles.

2.3 Characterization

2.3.1 Thermogravimetric Analysis (TGA)

A TA Instruments thermogravimetric analyzer Q500 was used for thermogravimetric analysis. The measurements were conducted in a continuous air environment at a flow rate of 60 mL min^{-1}.

2.3.2 Calcination

Calcination was conducted at a programmable muffle in a regulated air environment. According to the thermal decomposition characteristics identified using TGA, ZnONPs produced from *M. oleifera* leaf extract, *T. chebula* fruit extract, and *A. vera* gel were calcined at temperatures of 700 °C, 600 °C, and 500 °C, respectively. The thorough elimination of organic residues and improved crystallinity allowed the samples to cool naturally to ambient temperature within the furnace.

2.3.3 Dynamic Light Scattering (DLS)

The particle size distribution was assessed using the Litesizer™ 500 particle analyzer. The device uses a laser wavelength of 658 nm and incorporates backscattering detection at 175°, with measurements conducted at 25 °C. An aqueous dispersion of ZnONPs at 0.1 wt.% was subjected to ultrasonication for 15 min at 20 W using a probe-type ultrasonic homogenizer.

2.3.4 UV–Vis Spectroscopy

UV–Vis absorption was obtained using a Shimadzu UV-2600 double-beam spectrophotometer, functioning at a wavelength with a spectral bandwidth of 1 nm.

2.3.5 X-ray Diffraction

X-ray diffraction was obtained using a Bruker D8 Advance with Cu Kα radiation. Data was acquired over a 2θ range of 10–80° with a step increment of 0.02° at ambient temperature.

2.3.6 Scanning Electron Microscopy (SEM)

The morphological analysis of the fractured surfaces was carried out using a ZEISS Gemini SEM operated at an accelerating voltage of 10–15 kV. Samples were sputter-coated with a thin gold layer to prevent charging. Elemental composition was analyzed using an energy-dispersive X-ray spectroscopy (EDS) system at the same operating conditions, enabling simultaneous evaluation of surface morphology and elemental distribution.

2.3.7 Raman Spectroscopy

Raman spectra were obtained by HORIBA LabRAM HR Evolution Raman spectrometer integrated with an optical microscope. Excitation was delivered by a 785 nm laser functioning at 10 mW, and the spectra were acquired with a spectral resolution of approximately 4 cm^{-1} through four accumulations.

2.3.8 Attenuated Total Reflectance Fourier Transform Infrared (ATR–FTIR) Spectroscopy

The spectra were obtained using a Bruker Tensor 27 FTIR spectrometer fitted with a diamond ATR attachment. Spectra were acquired within the range of 4000–400 cm^{-1} at a spectral resolution of 4 cm^{-1}, averaging 64 scans.

2.4 Photocatalytic Activity of ZnO

The photocatalytic activity was evaluated in a quartz reactor containing an aqueous suspension of ZnO nanoparticles, methyl orange (MO), and deionized water at a molar ratio of 1:4.5:8. Prior to irradiation, the suspension (1 mL) was magnetically stirred in the

absence of light for 30 min to achieve adsorption–desorption equilibrium. The reaction mixture was subsequently irradiated with a UV lamp emitting at 365 nm with an incident light intensity of approximately 1.0 mW cm^{-2}. Photocatalytic degradation tests were performed for 180 min, with aliquots extracted at 30-minute intervals.

2.5 SERS-based Spectroscopic Investigation (SERS)

L-phenylalanine was dissolved in distilled water to obtain a 10^{-3} mol/L. The ZnONPs were combined with *L*-Phe and incubated for 1 day before measurement.

Surface-enhanced Raman scattering (SERS) with spectral resolution of approximately 4 cm^{-1} was obtained using the HORIBA LabRAM HR Evolution Raman microscope, which is equipped with an optical microscope. Excitation was delivered with a 785 nm diode laser functioning at an output power of 10 mW, with an exposure duration of 40 s for each accumulation. Nine spectra were obtained from three distinct sites on three different drops of ZnO NP/*L*-phenylalanine (*L*-Phe). No spectrum characteristics linked to laser-induced deterioration were detected.

2.6 Spectral Evaluation

Spectral data were processed and assessed with OriginPro software, including baseline correction, peak fitting, and data smoothing techniques.

All synthesis experiments and photocatalytic measurements were performed in triplicate (n = 3) to ensure reproducibility. Photocatalytic degradation experiments were conducted for 180 min under 365 nm UV irradiation with an intensity of ~1.0 mW cm^{-2}, and aliquots were collected at 30 min intervals. The reported results represent the average values of three independent experiments, and the observed experimental variation was less than ±3%, confirming the reliability of the experimental procedure.

3. RESULTS AND DISCUSSION

3.1 Spectroscopic Methods

A periodic and systematic atomic structure displays distinct and precise diffraction in X-ray diffraction patterns. Conversely, weakly crystalline or amorphous materials exhibit diffuse and broad halos rather than distinct reflections. This work reveals that XRD patterns of produced ZnONPs (Fig. 1) demonstrate a low level of amorphous or crystallinity characteristics. Neem fruit pulp–mediated ZnO nanoparticles were confirmed by XRD with ~42 nm crystallite size and ~35.5 nm particles, as observed by prior studies (Alampally *et al.* 2025).

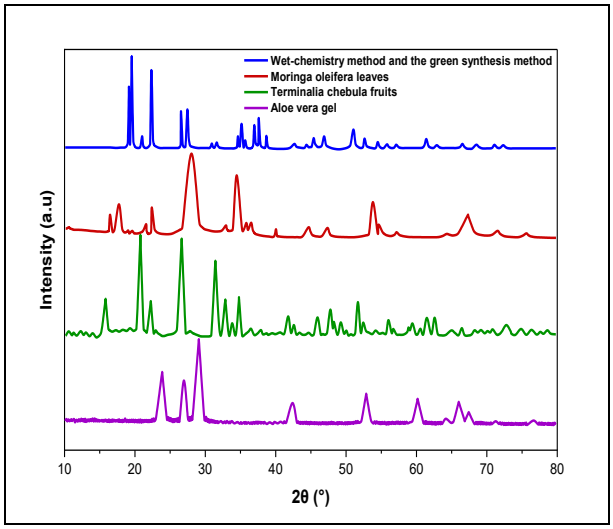


Fig. 1: XRD patterns of ZnONPs synthesized by wet-chemical and green synthesis methods using *Moringa oleifera*, *Terminalia chebula*, and *Aloe vera* extracts, confirming the formation of hexagonal wurtzite ZnO structure

Consequently, all materials underwent calcination for additional structural analysis. TGA was conducted to ascertain the appropriate calcination temperature for the formation of ZnO nanoparticles. Fig. 2 displays TGA curves for the analyzed ZnO samples. The ZnONPs synthesized by the wet chemical method have a unique thermal degradation profile in contrast to others, which were produced by green methods utilizing extracts from *M. oleifera* leaves, *T. chebula* fruits, and *A. vera* gel. The extracts exhibit a progressive three-step weight reduction, mainly due to the desorption of physically adsorbed moisture, the breakdown of organic phytochemicals, and the removal of remaining hydroxyl groups. Conversely, ZnONPs exhibit a fast mass drop between 350–400 °C, resulting in an approximately 26% to 18% weight loss linked to the breakdown of zinc hydroxide and zinc precursor intermediates into crystalline ZnO. A modest mass increase of approximately 5% observed between 400–600 °C can be ascribed to lattice stabilization and oxygen incorporation inside the ZnO structure, succeeded by an additional weight loss of around 3% at 600 °C due to the elimination of residual surface hydroxyl species. In light of these data, ZnONPs were calcined at 600 °C and 400 °C to enhance crystallinity and thermal stability.

Stage 1 corresponds to dehydration, leading to negligible mass reductions of 4% (ZnONPs–MO), 6% (ZnONPs–TC), and 6% (ZnONPs–AV). Stage 2 involves progressive dehydroxylation at temperatures of 150–700 °C, 150–600 °C, and 150–500 °C, with the oxidation of residues from plant extracts, resulting in the formation of CO_2 and H_2O. The corresponding weight reductions are 32%, 26%, and 21%. Stage 3, commencing at 600–700 °C, entails a weight loss of less than 2%, signifying the

stability of crystalline phases. According to the findings, calcination temperatures were established at 600 °C for ZnONPs–A' and ZnONPs–MO, 700 °C for ZnONPs–A, and 500 °C for ZnONPs–AV. The obtained diffraction patterns are illustrated in Figure 3.

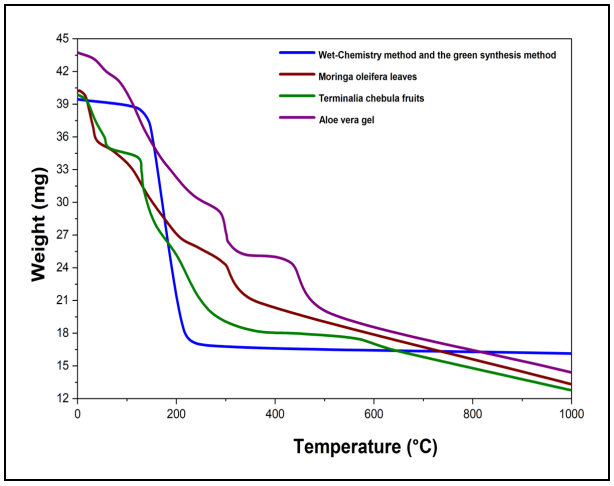


Fig. 2: TGA curves of ZnONPs synthesized by wet-chemical and green synthesis methods showing weight-loss stages corresponding to moisture removal, phytochemical decomposition, and ZnO crystallization

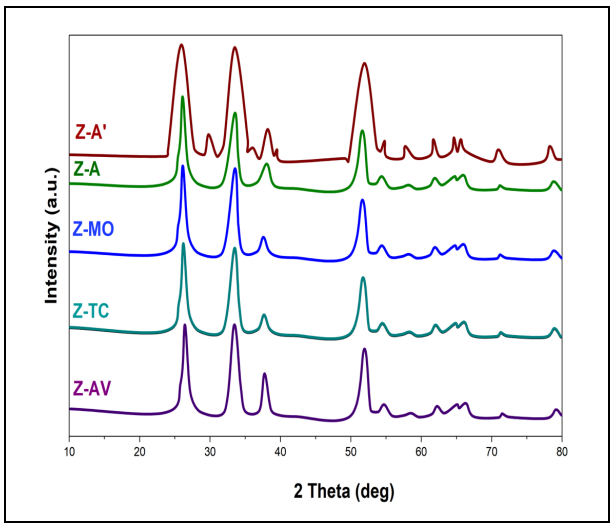


Fig. 3: X-ray diffraction (XRD) patterns of calcined ZnONPs synthesized by the wet-chemical method (A, calcined at 400°C and A', at 600 °C), and by the green chemistry method using extracts from *M. oleifera* (MO) leaves, *T. chebula* (TC) fruits, and *A. vera* (AV) gel

Fig. 3 illustrates the XRD patterns of calcined ZnONPs corresponding to hexagonal wurtzite-type ZnO phase lattice parameters of $a = b = 3.25$ Å and $c = 5.20$ Å. Lack of peaks from alternative zinc oxides or metallic zinc corroborates the elevated phase purity of the produced ZnONPs. The narrow full width and elevated intensity at half maximum signify a well-crystallized sample. A FWHM exhibits a slight rise at subsequent orders: ZnONPs–MO < ZnONPs–A < ZnONPs–A' < ZnONPs–TC < ZnONPs–AV, indicating progressive reduction in crystallite size.

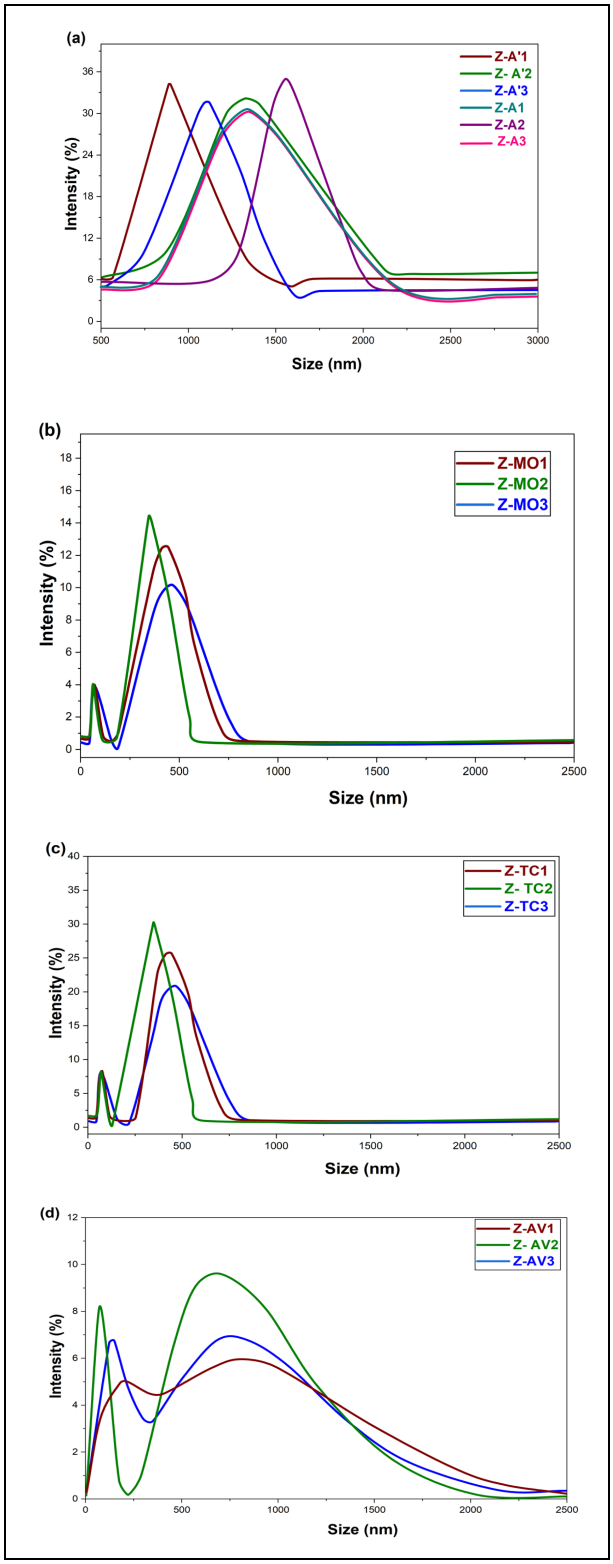


Fig. 4: (a) DLS analysis of calcined ZnONPs s: (a) synthesized via the wet-chemistry method (A, calcined at 400 °C and A', at 600 °C), and by the green chemistry method using extracts from (b) *M. oleifera* leaves, (c) *T. chebula* fruits, and (d) *A. vera* gel

The ZnONPs–A calcined at 600 ℃ have a (101) diffraction intensity approximately 25% greater than that of (110) reflection, indicating growth in the (101) direction. Conversely, ZnONPs–A' (400 ℃) and green-synthesized material exhibit a predominant (110) reflection, signifying preferred exposure as (110) surface. Crystallite dimensions were calculated via the Debye–Scherrer equation, and the findings are presented in Table 1.

DLS studies were performed in triplicate for all ZnONPs suspensions to verify the reproducibility of particle size distribution profiles. Minor discrepancies were noted among successive measurements. The initial measurement, indicating "biggest population", was labeled as "1". During phases two and three, the nanoparticles experienced gravity settling, leading to a reduction in hydrodynamic diameter.

Table 1. Surface evaluation outcomes of calcined ZnONPs

ZnONPs	Planes (hkl)	XRD		DLS Average Particle Size in Suspension [nm]	EDS [keV]		Atomic Content [%]	λ_{abs} [nm]	UV–Vis, E_g [eV]	Catalytic Efficiency [%]
		2θ	Crystallite Size [nm]							
$ZnONP-A'$ (400°C) $ZnONPs-A$ (600 °C)	110	26.63	42.8	1500 1600 450	O Kα – 0.52	O: 49.1	291	4.26 4.12	33.4 60.5	110 101 110
	101	33.93	32		Zn Lα – 1.01	Zn: 50.9				
	110	26.64	44.3		O Kα – 0.52	O: 46.3	301			
	101	33.94	44.3		Zn Lα – 1.01	Zn: 53.7				101
	110	26.64	76.4		O Kα – 0.51	O: 56.8	325	3.81	68.6	110
	101	33.96	65.9		Zn Lα – 1.01	Zn: 43.2				101
$ZnONPs-MO$ (*M. oleifera*, 700 °C)	110	26.68	27	500	O Kα – 0.52	O: 54.2	283	4.38	63.5	110
	101	34	28.9		Zn Lα – 1.01	Zn: 45.8				101
	110	26.65	17.1	850	O Kα – 0.51	O: 44.9	270	4.59	52.1	110
$ZnONPs-TC$ (*T. chebula*, 600°C)	101	33.96	19.3		Zn Lα – 1.01	Zn: 55.1				101
	110	26.63	42.8	1500	O Kα – 0.52	O: 49.1	291	4.26	33.4	110
	101	33.93	32		Zn Lα – 1.01	Zn: 50.9				101
$ZnONPs-AV$ (*A. vera*, 500°C)	110	26.6515	17.13	263	0.51	OK_α	O: 42.81	270	4.59	52.1
					3.44	Zn L_α	Zn:			
	101	33.9552	19.30		3.68	ZnL_β	39.87			

The spherical nanoparticles were uniformly dispersed and formed agglomerates. This aggregation can be ascribed to favorable van der Waals and electrostatic interactions.

Fig. 5 shows the SEM images of the wet-chemically synthesized ZnONPs, which reveal predominantly spherical particles forming agglomerated clusters. At 400 °C, the particles appear smaller and loosely packed with noticeable surface irregularity, indicating limited grain growth and incomplete densification. In contrast, the 600 °C sample exhibits more compact and coalesced agglomerates due to enhanced crystallization and partial sintering. The corresponding EDS spectra confirm the exclusive presence of Zn and O elements without detectable impurities. Slight deviations from the ideal O:Zn (2:1) ratio are observed, which are typical for EDS analysis of

metal oxides. The increased Zn proportion at 600 °C correlates with improved crystallinity and structural densification, while the relatively higher oxygen content at 400 °C may be associated with surface hydroxyl groups or incomplete oxidation.

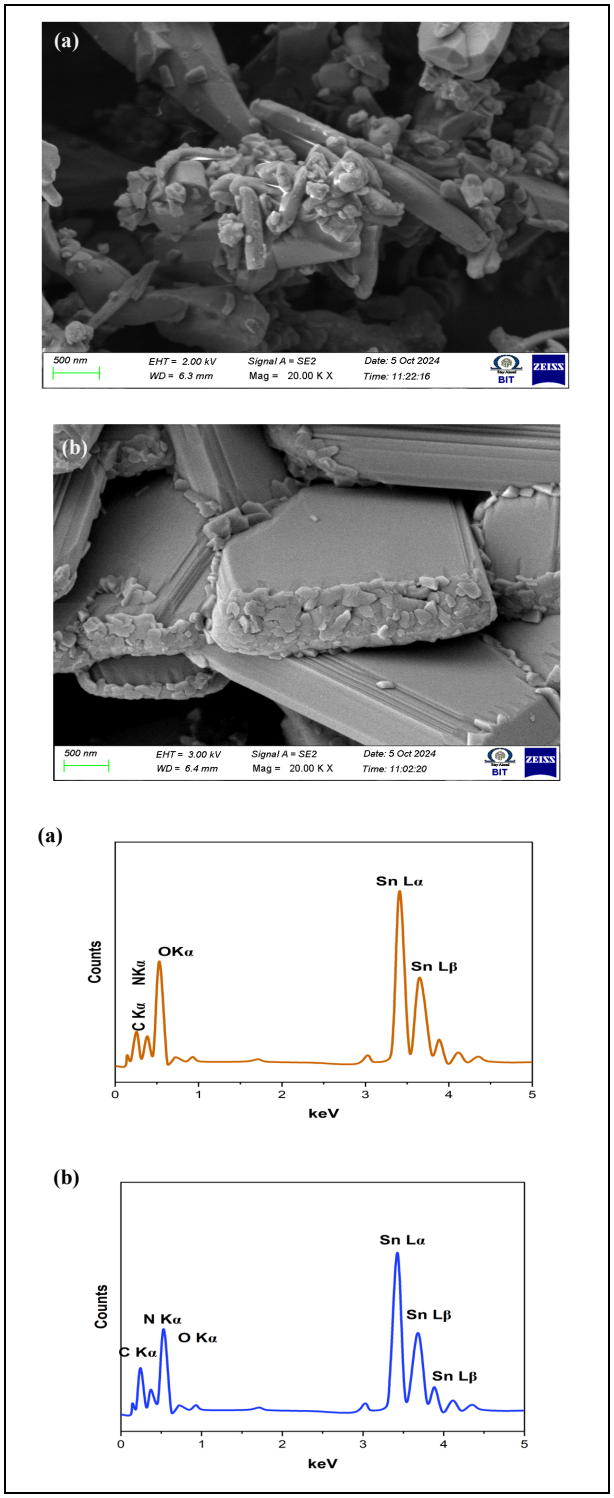


Fig. 5: SEM micrographs and SEM–EDS analysis of wet-chemically synthesized ZnONPs showing spherical particle morphology and calcined at 400 °C (a) and at 600 °C (b), confirming the elemental composition

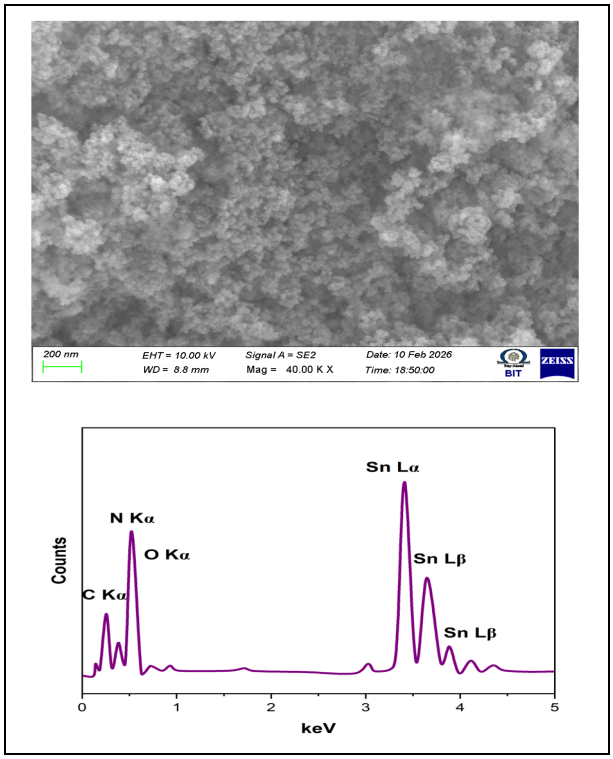


Fig. 6: SEM micrograph and EDS analysis of ZnONPs synthesized using *M. oleifera* leaf extract and calcined at 700 °C

SEM micrographs of the *M. oleifera*-derived ZnONPs show well-developed, uniformly distributed spherical grains with moderate agglomeration, as shown in Fig. 6. The higher calcination temperature (700 °C) promotes significant grain growth, resulting in clearly defined particle boundaries and textured surfaces that enhance active surface area. EDS analysis confirms high phase purity with only Zn and O peaks detected. The relatively higher oxygen atomic percentage suggests oxygen-rich surface states or vacancy-related defect structures typical of green synthesis routes. The combination of improved crystallinity and defect-assisted surface characteristics likely contributes to the superior photocatalytic performance observed for this sample.

Fig. 7 shows the SEM morphology of the *T. chebula* fruit-mediated ZnONPs, which consist of medium-sized spherical to slightly irregular particles forming nano-clustered aggregates with moderate porosity. Grain boundaries are distinguishable, indicating controlled nucleation and growth during plant-assisted synthesis. The EDS spectrum confirms the exclusive presence of Zn and O elements. The measured atomic percentages show moderate deviation from ideal stoichiometry, suggesting partial oxygen deficiency (ZnO_x). This balanced composition, combined with uniform morphology, reflects effective phytochemical stabilization during synthesis and contributes to stable structural and catalytic properties.

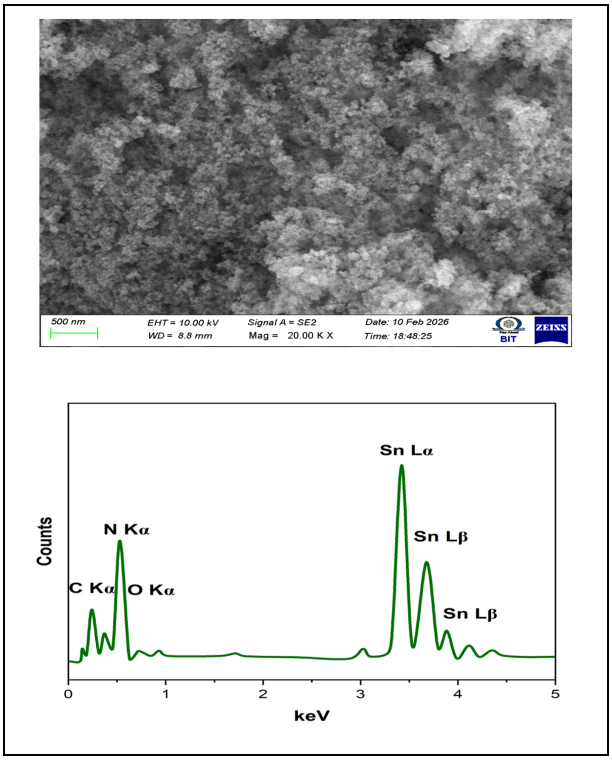


Fig. 7: SEM micrograph and EDS analysis of ZnONPs synthesized using *T. chebula* fruit extract and calcined at 600 °C

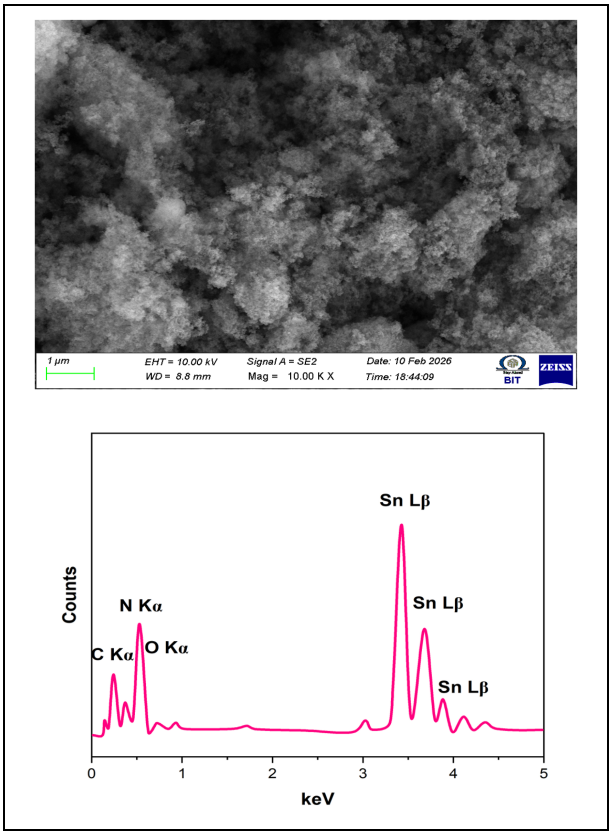


Fig. 8: SEM micrograph and EDS analysis of ZnONPs synthesized using *A. vera* gel extract and calcined at 500 °C

SEM analysis of the *Aloe vera* gel extract-derived ZnONPs (Fig. 8) reveals very fine particles forming densely packed agglomerates, consistent with limited grain growth at the lower calcination temperature (500 °C). The morphology indicates high surface area and elevated grain boundary density, promoting aggregation due to high surface energy. EDS results confirm phase purity with only Zn and O peaks present. This sample exhibits comparatively higher Zn atomic percentage and lower oxygen content, indicating a more oxygen-deficient structure. The observed non-stoichiometry is consistent with low-temperature crystallization and may enhance defect-mediated optical and catalytic behavior.

EDS profiles further substantiate the production of ZnO. Each spectrum displays four distinctive peaks within the 0.5–4.0 keV region. Table 1 enumerates respective energies for all oxides. Minor peaks of around 0.39 keV (N Kα) and 0.26 keV (C Kα) were detected in all samples and were attributed to residual gases within the SEM chamber.

Atomic percentages of Zn and O presented in Table 1 exhibit significant discrepancies from the ideal stoichiometric ratio of ZnO (O:Zn = 1:1). The quantified values are O = 50.82 wt.% / Zn = 49.18 wt.%, O = 49.67 wt.% / Zn = 50.33 wt.%, O = 52.41 wt.% / Zn = 47.59 wt.%, O = 51.36 wt.% / Zn = 48.64 wt.%, and O = 48.92 wt.% / Zn = 51.08 wt.% for ZnO nanoparticles produced using various methods. These discrepancies align with values frequently documented in the literature for EDS-based elemental analysis of ZnO nanoparticles, where the quantified oxygen content typically varies widely based on manufacturing technique, surface chemistry, particle size, and measurement conditions. Specifically, EDS analyses often indicate oxygen concentrations between around 40 and 80 atomic percent, whereas zinc concentrations generally span from 20 to 60 atomic percent, due to instrumental and methodological constraints. The disparities can be mainly ascribed to the reduced sensitivity of EDS to light elements like oxygen, surface hydroxylation or adsorbed species, substrate contributions, matrix effects, and variations in quantification techniques. Moreover, the comparatively substantial interaction volume and restricted surface sensitivity of EDS, in contrast to techniques like X-ray photoelectron spectroscopy (XPS), further exacerbate non-ideal Zn/O ratios. Consequently, deviations from the theoretical 1:1 Zn/O atomic ratio are frequently noted and should be regarded as standard in SEM–EDS analysis of ZnONPs.

An increasing number of studies suggest that the synthesis method significantly influences the extent of non-stoichiometry in ZnO. Plant extracts are abundant in polyphenols, carbohydrates, and phytochemicals, as well as other proteins, which can establish locally reducing and oxygen-deprived conditions at crystal formation and

nucleation. These conditions promote the creation of oxygen vacancies and zinc interstitial defects, both of which are recognized contributors to non-stoichiometry in ZnO. As a result, green-synthesized ZnO nanoparticles often display defect-related spectral characteristics, such as vacancy-associated emissions in photoluminescence (PL) spectra, paramagnetic signals in electron paramagnetic resonance (EPR), and distinctive shifts or asymmetry in O 1s and Zn 2p in X-ray photoelectron spectroscopy. Furthermore, low-temperature wet-chemical and biosynthetic techniques typically lack adequate thermal energy and oxygen diffusion to completely eradicate defect states, therefore maintaining oxygen-deficient ZnO_{-x} phases.

The degree of non-stoichiometry at ZnO is influenced not only by the synthesis method but also by parameters like temperature, oxygen pressure, the inclusion of reducing agents, and post-treatment methods. High temperatures in oxygen-rich environments facilitate vacancy elimination and re-oxidation, driving material towards stoichiometric ZnO, while low-temperature synthesis under restricted oxygen conditions promotes the stabilization as oxygen-deficient ZnOx.

The ATR-FTIR of calcined ZnONPs displays distinct absorption bands at 681.1, 618.3, and 552.4 cm^{-1}, corresponding to Zn–O lattice vibrations within the wurtzite ZnO structure. Bands at 500–700 cm^{-1} were typically attributed to Zn–O stretching modes, encompassing longitudinal optical (LO) and transverse optical (TO) phonon vibrations linked to Zn–O–Zn bonding networks. Comparable studies have documented absorption patterns in the range of 610–630 cm^{-1} and 500–600 cm^{-1}, which are ascribed to the fundamental vibrational modes of Zn–O. Subtle alterations in peak locations compared to documented values (generally ~600–650 cm^{-1}) can be attributed to fluctuations in particle size, crystallinity, defect density (oxygen vacancies), morphology, and variations in calcination temperature. The measured FTIR characteristics align well with previously documented spectra of ZnO produced using wet-chemical and green methods, calcined at temperatures between 500 and 700 °C. Variations in band locations and intensities observed in other investigations are likely attributable to changes in phase purity, defect density, stoichiometry (ZnO_{-x}), and microstructural attributes of the ZnO nanoparticles.

ZnO primarily crystallizes in the hexagonal wurtzite form, classified under the space group $P6_3mc$ (No. 186) with C_{6v}^4 point-group symmetry. The primitive unit cell has two Zn^{2+} cations and two O^{2-} anions, each coordinated in a tetrahedral arrangement. Group-theoretical analysis forecasts the subsequent optical phonon at the Γ point of the Brillouin zone: $\Gamma = A_1 + 2B_1 + E_1 + 2E_2$. A_1 and E_1 are polar modes that split into longitudinal optical (LO) and transverse optical (TO) components, whereas E_2 (high) and E_2 (low) are nonpolar modes. Raman-active modes were linked to lattice vibrations of the Zn and O sublattices, respectively. The B_1 modes are silent (inactive in both Raman and infrared spectra). Thus, the Raman-active modes of wurtzite ZnO are A_1, E_1, and E_2, with the E_2 (high) mode serving as a distinctive marker of highly crystalline ZnO.

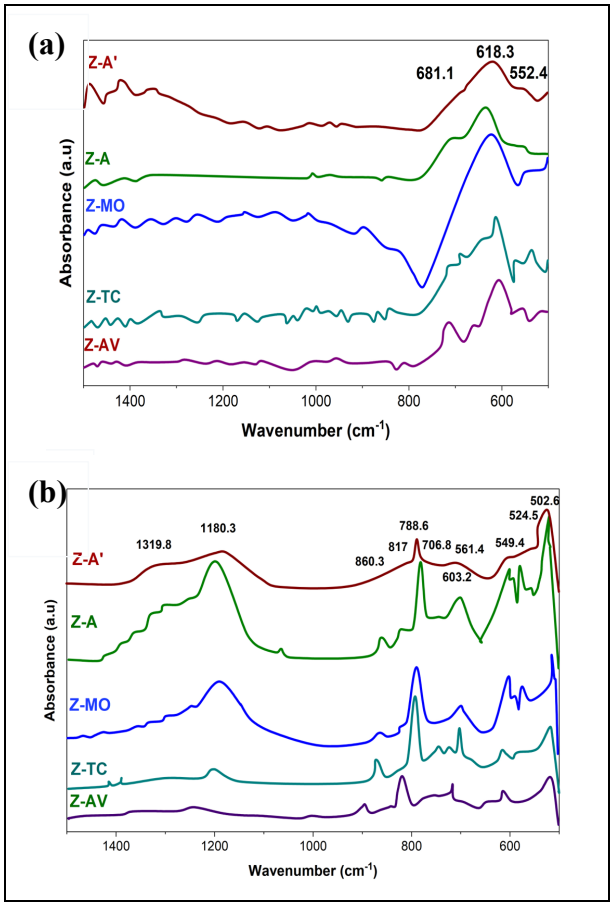


Fig. 9: ATR-FTIR (a) and Raman (b) spectra of calcined ZnONPs synthesized via the wet-chemical method (calcined at 400 °C and 600 °C) and the green synthesis method using the three extracts

The Raman spectra display distinct bands at around 502.6, 561.4, 788.6, and 860.3 cm^{-1}, indicative of wurtzite ZnO. The pronounced peak at approximately 502.6 cm^{-1} is attributed to the E_2 (low) mode, primarily linked to vibrations of the Zn sublattice, whereas the band at around 706.8 cm^{-1} corresponds to the E_2 (high) mode, a characteristic vibration at the ZnO lattice resulting mainly from oxygen atom vibrations and indicative of superior crystallinity. The elevated wavenumber characteristics detected at around 788.6 cm^{-1} and 860.3 cm^{-1} are ascribed to longitudinal optical (LO) phonon modes, specifically A_1(LO) and E_1(LO), which are frequently stimulated or intensified by defects, oxygen vacancies, lattice disorder, or finite-size effects in ZnO nanoparticles. The E_2 (high) mode is generally crisp and strong in larger, highly crystalline ZnO particles, but it

broadens and exhibits subtle red shifts with decreasing particle size.

Raman characteristics at around 502.6 and 524.5 cm^{-1} were detected in ZnO nanoparticles produced using the wet-chemical method using *M. oleifera* extract. The band at around 502.6 cm^{-1} can be ascribed to the E_2 (low) mode, principally linked to vibrations of the Zn sublattice, and is responsive to lattice strain and particle size influences. The less prominent feature at approximately 549.4 cm^{-1}, observed solely in ZnO–A calcined at 400 °C, may be linked to defect-activated or disorder-induced vibrational modes, which typically arise in nanocrystalline ZnO due to oxygen vacancies, surface disorder, or lattice distortions, especially at reduced calcination temperatures.

Fig. 10 illustrates the UV–Vis spectra of calcined ZnONPs within 200–600 nm wavelength. Absorption edge, indicative of bandgap changes, is observed in the ultraviolet area. The measurements demonstrate a blue shift relative to the prediction for tetragonal rutile ZnO and previously documented 2D nanosheets and ZnO nanoparticles produced by solvothermal methods. The red shift for hydrothermally synthesized ZnONPs (λabs = 301.7 nm, 11–12 nm) is also apparent. The outcomes were consistent with documented statistics for ZnO. The detected blue shift by reduced nanoparticle size validates the quantum confinement effect, indicating that the bandgap energy of calcined ZnONPs rises inversely with particle size.

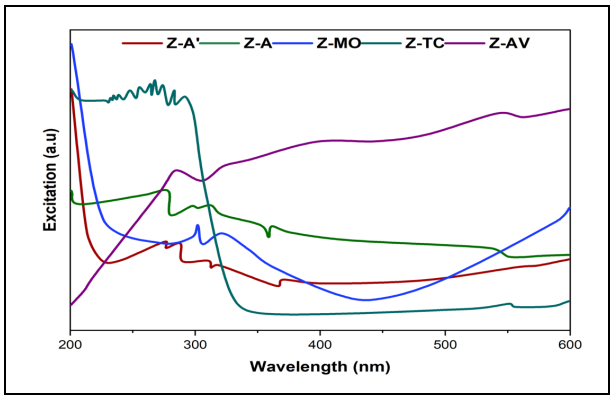
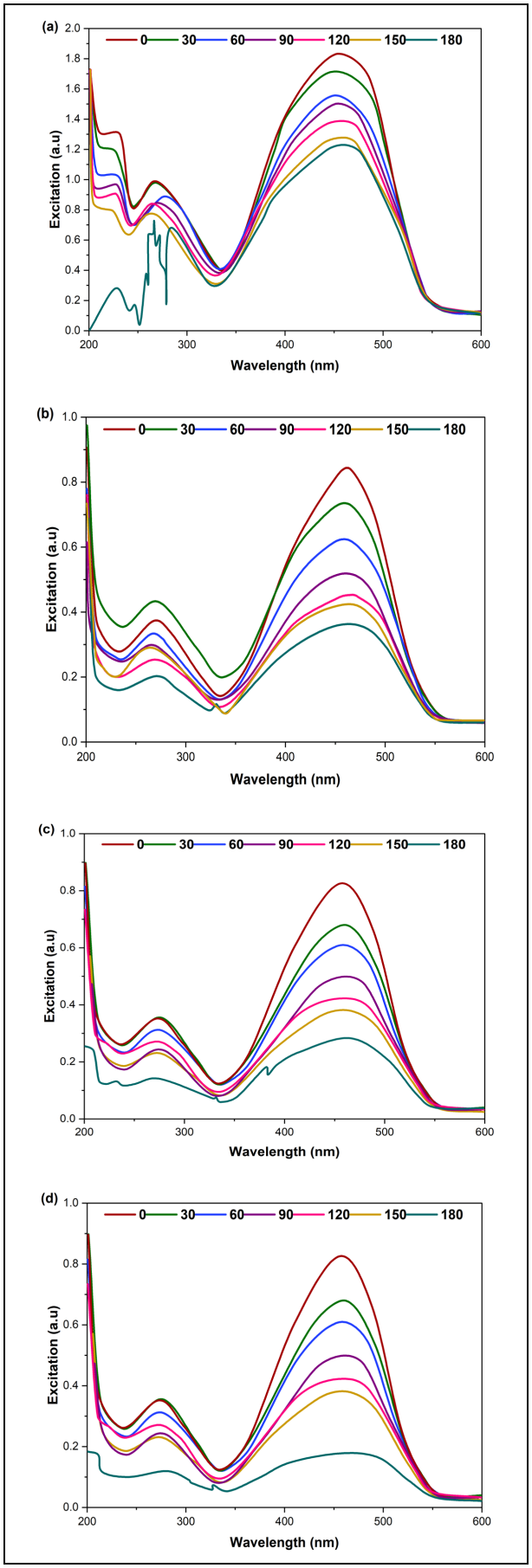


Fig. 10: UV–Vis spectra of wet-synthesized ZnONPs (calcined at 400 °C and 600 °C), and Moringa-mediated, Terminalia-mediated, and Aloe-mediated green ZnONPs

3.2 Photocatalytic Activity

Fig. 11 illustrates time-dependent spectra of methyl orange (MO), a widely used synthetic azo dye. MO was employed to assess the photocatalytic efficacy of ZnONPs at 365 nm light irradiation. The mixture, including ZnONPs, MO, and deionized water at a molar ratio of roughly 1:4.5:8, was subjected to irradiation. The spectra were obtained at 30 min intervals over a 180 min irradiation period.



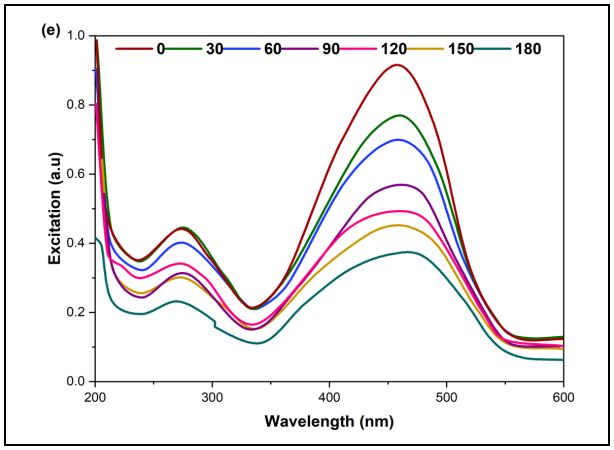


Fig. 11: Photodegradation efficiency of calcined ZnONPs synthesized via the wet-chemistry method (Calcined at 400 °C and 600 °C, a and b) and the green chemistry method using extracts from *M. oleifera* (c), *T. chebula* (d), and *A. vera* (e)

The ZnONPs synthesized from *M. oleifera* leaf extract, possessing an average crystallite size of 17.2 nm, demonstrated the best photocatalytic performance, achieving a degradation of 67% of MO at 180 min. In contrast, ZnONPs with *Aloe vera* extract, exhibiting a crystallite size of 21.8 nm, attained a degradation efficiency of 60%, whilst the NPs derived from *T. chebula* fruit extract, with a crystallite size of 32.4 nm, demonstrated 35% degradation efficiency. Green-synthesized pure, Al-doped, and Al-ZnO/rGO nanocomposites displayed enhanced photocatalytic and anticancer performance due to improved charge separation and reduced bandgap, as reported by Alaizeri *et al.* (2026). The photocatalytic performance of the synthesized ZnONPs is consistent with previously reported ZnO-based photocatalysts synthesized via green routes, which also demonstrate effective catalytic activity for dye degradation and environmental remediation applications (Almohana *et al.* 2025).

The photocatalytic and SERS performance of ZnONPs is strongly influenced by structural defects such as oxygen vacancies (V_o), zinc interstitials (Zn_i), and surface defect states. These defects introduce intermediate electronic energy levels within the bandgap of ZnO, which facilitate the trapping of photogenerated electrons and holes during UV irradiation. As a result, recombination of electron–hole pairs is suppressed, enabling the generation of reactive oxygen species (ROS) such as OH and O_2^- radicals, which play a critical role in the degradation of organic dye molecules like methyl orange (MO).

ZnONPs synthesized by the wet chemical technique exhibited degradation efficiencies of 61% and 32%, with crystallite diameters of 48.6 and 36.7 nm. Table 1 encapsulates the photocatalytic efficiency of the examined ZnONPs.

3.3 Adsorption Monitored by SERS

ZnO was typically classified as a non-plasmonic semiconductor, resulting in markedly less surface-enhanced Raman scattering activity relative to noble metals like silver (Ag) and gold (Au). Thus, efficient SERS amplification on ZnO nanostructures typically depends on ultraviolet excitation or the creation of hybrid systems, whereby ZnO is coated, adorned, or combined with noble metals to leverage localized surface plasmon resonance (LSPR)–induced electromagnetic enhancement. In these hybrid structures, the intensified electromagnetic field produced at the noble metal surface infiltrates the ZnO–adsorbate contact, facilitating Raman signal enhancement. Conversely, pure ZnO-based SERS primarily functions by a chemical (charge-transfer) enhancement process, which entails photo-induced electron transfer between ZnO defect states and adsorbed molecules. Conversely, a restricted number of studies have evidenced the application of pure ZnO nanoparticles as SERS-active substrates.

Fig. 12 displays the SERS spectrum of *L*-Phe adsorbed onto ZnONPs, which were produced using *M. oleifera* leaf extract and calcined at 600 °C. The nanoparticles were chosen for their exceptional photocatalytic efficacy at the destruction of MO, indicating a high concentration of surface defect states conducive to charge-transfer interactions. The spectrum displays intensified bands at 308.2 (ν_8a, ν_8b), 431.3 (ν_{14}), 495.6 (ν_7a), 602.3, and 704.2 cm^{-1} (ν_{10}a), which correspond to the distinctive vibrational modes of the aromatic ring of *L*-Phe.

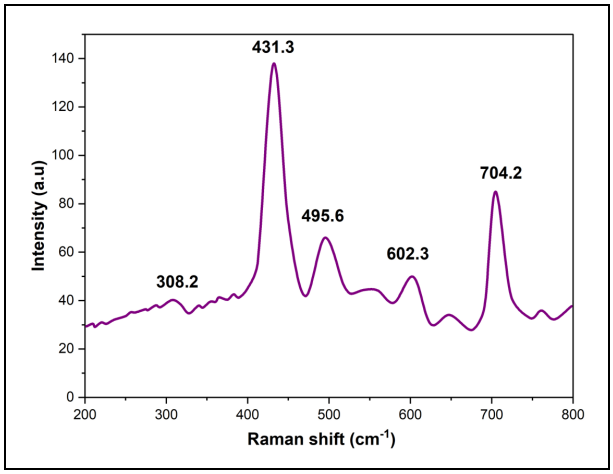


Fig. 12: SERS response of *L*-phenylalanine at *Moringa*-derived ZnONPs

An in-depth examination of intensities, band locations, and the width half maximum, especially concerning the ν_{12} mode, elucidates the adsorption of *L*-Phe. In comparison to standard Raman spectra, the ν_{12} band demonstrates a red shift of roughly 8 cm^{-1}, significant broadening (ΔFWHM = +4 cm^{-1}), and

diminished relative amplification, indicating tilted orientation of the phenyl ring at the ZnONP surface. Furthermore, two prominent features at approximately 431.3 and 602.3 cm^{-1}, attributed to $\nu_s(COO^-)$ and $\nu(CH_2)$ vibrations, respectively, reinforce a configuration wherein the aliphatic chain and carboxylate group are directed towards the ZnO surface, while the aromatic ring is partially tilted. As reported in previous studies, the Raman spectroscopy confirmed the successful formation of carbon dot-adorned silver nanoparticles, exhibiting characteristic D and G bands of carbon dots along with vibrational features associated with AgNP interactions (Suguna *et al.* 2022).

Similarly, in SERS experiments, defect sites present on the ZnO nanoparticle surface promote charge-transfer interactions between the semiconductor surface and the adsorbed *L*-phenylalanine molecules. This defect-assisted charge transfer enhances the Raman scattering intensity by increasing the polarizability of the adsorbed molecules. Therefore, the presence of oxygen vacancies and defect-related surface states not only improves photocatalytic degradation efficiency but also contributes to the observed Raman signal enhancement in ZnO-based SERS substrates.

These data underscore that adsorption geometry and molecule orientation in SERS are highly reliant on the substrate. *L*-phenylalanine predominantly interacts with ZnO and Zn nanoparticles on Ag nanoparticles through its aromatic ring, while the carboxyl group and aromatic ring facilitate adsorption. In the case of MgO nanoparticles, the interactions involve the amino group and aromatic ring, whereas on Au nanoparticles and iron oxide nanostructures, simultaneous coordination occurs through the amino group, carboxyl group, and aromatic ring.

4. CONCLUSION

Zinc oxide nanoparticles were successfully synthesized through both conventional wet-chemical and plant-mediated green synthesis routes using *Moringa oleifera*, *Terminalia chebula*, and *Aloe vera* extracts. Structural characterization confirmed the formation of hexagonal wurtzite ZnO with crystallite sizes ranging from 11.1 to 72.2 nm and bandgap energies between 3.11 and 4.22 eV, indicating strong size-dependent optical behavior. Among the synthesized samples, the *M. oleifera*-mediated ZnONPs exhibited the highest photocatalytic performance, achieving 67% degradation of methyl orange within 180 min under 365 nm UV irradiation, while *A. vera*, *T. chebula*, and wet-chemical ZnO samples showed comparatively lower efficiencies. SERS investigations using *L*-phenylalanine demonstrated a Raman signal enhancement factor of approximately 10^2, confirming the sensing capability of the synthesized nanoparticles. The results demonstrate that green synthesis offers several advantages over conventional chemical routes, including eco-friendly processing, reduced use of hazardous reagents, and the formation of defect-rich ZnO nanostructures that enhance photocatalytic and sensing performance. These findings highlight the potential of plant-mediated ZnO nanoparticles as multifunctional materials for environmental remediation and sensing applications. Future studies could focus on biocompatibility evaluation, biomedical applications such as bone regeneration systems, and the development of practical ZnO-based photocatalytic and SERS sensors for real-world environmental monitoring.

FUNDING

This research received no specific grant from any funding agency in the public, commercial, or not-for-profit sectors.

CONFLICTS OF INTEREST

The authors declare that there is no conflict of interest.

COPYRIGHT

This article is an open-access article distributed under the terms and conditions of the Creative Commons Attribution (CC BY) license (http://creativecommons.org/licenses/by/4.0/).

REFERENCES

Ahmadi, B. S., Abdoos, H. and Karimzadeh, F., Green synthesis of ZnO@ZnS core–shell nanoparticles for detection of lead and iron ions in aqueous solutions by colorimetric paper sensors, *Chem. Pap.*, 76(1), 99–109(2022). https://doi.org/10.1007/s11696-021-01840-3

Alaizeri, Z. A. M., Ali, S. M. and Alhadlaq, H. A., Tailored Al-doped ZnO/rGO nanocomposites for enhanced anticancer and photocatalytic activities: a green synthesis approach, *Res. Chem. Intermed.*, 52(1), 19–46(2026). https://doi.org/10.1007/s11164-025-05790-3

Alampally, B. B., Pidamarthi, S., Gandamalla, S., Subba Rao, Y. and Durga Bhavani, A. K., Neem fruit pulp extract mediated biosynthesis, characterization of zinc oxide nanoparticles, and evaluation of their antioxidant, anticancer, and catalytic properties, *Res. Chem.*, 18(2025). https://doi.org/10.1016/j.rechem.2025.102697

Almohana, A. G., Almayahi, B. A., Alkelaby, K. K. and Abdullah, C. A. C., Structural and functional characterization of green-synthesized zinc oxide nanoparticles for biomedical applications, *Nano-Struct. Nano-Obj.*, 43, 101526(2025). https://doi.org/10.1016/j.nanoso.2025.101526

Almoneef, M. M., Awad, M. A., Aldosari, H. H., Hendi, A. A., Alshammari, S. G., Aldehish, H. A., Merghani, N. M., Alsahli, A. M., Almutairi, B. M., Alharbi, R. M., Almlla, A. A. and Aljazeeri, J. M., Eco-friendly synthesis of magnetic ZnO/Fe_3O_4 nanocomposites: Structural, morphological, antimicrobial, and anticancer evaluation, *J. Sci. Adv. Mater. Dev.*, 10(3), 100921 (2025). https://doi.org/10.1016/j.jsamd.2025.100921

Begum, T., Agarwal, S., Bhuyan, P., Das, J., Verma, A. K., Guha, A. and Ganguly, M., *Aloe vera* gel mediated green synthesis of ruthenium nanoparticles and their potential anticancer activity, *Next Nanotechnol.*, 7, 100095(2025). https://doi.org/10.1016/j.nxnano.2024.100095

Chhetri, B. R., Jha, S., Bhattacharyya, N. K., Dolma, K. G. and Das, A. M., Green Synthesis and Characterization of Ag/ZnO Bimetallic Nanocomposites Using Evodia fraxinifolia Fruit Extract: Evaluation of Photocatalytic, Antimicrobial and Antioxidant Activities, *Asian J. Chem.*, 37(12), 3116–3126(2025). https://doi.org/10.14233/ajchem.2025.34753

Devi, V. N. M. and Shakitha, K., Eco-friendly synthesis of ZnO nanoparticles using *Moringa oleifera* leaf extract with enhanced antibacterial activity and in silico approach, *Sustain. Chem. One World*, 9, 100198(2026). https://doi.org/10.1016/j.scowo.2026.100198

Elsadek, M. F. and Al-Numair, K. S., Profiling of phytochemical constituents of *Terminalia chebula* fruit extract by different solvent effects and synchronized analysis of FTIR and GCMS, *J. King Saud Univers. Sci.*, 36(9), 103414(2024). https://doi.org/10.1016/j.jksus.2024.103414

Errico, V., Arrabito, G., Plant, S. R., Medaglia, P. G., Palmer, R. E. and Falconi, C., Chromium inhibition and size-selected Au nanocluster catalysis for the solution growth of low-density ZnO nanowires, *Sci. Rep.*, 5(1), 12336(2015). https://doi.org/10.1038/srep12336

Hasanin, M. S., Mahmoud, E. R. I., Al-Qabandi, O. A., Bassyouni, M. and Al Kiey, S. A., Eco-friendly Bi_2O_3 nanocomposite films based on cellulose acetate and carboxymethyl cellulose: A bioinspired approach for antimicrobial and biocompatible materials, *Int. J. Bio. Macromol.*, 333, 148721(2025). https://doi.org/10.1016/j.ijbiomac.2025.148721

Ibupoto, M. H., Ujjan, S. H. and Tahira, A., Green Synthesis of ZnO Nanostructures and Their Antibacterial Activity Against Catfish Pathogen, *Pakistan J. Anal. Environ. Chem.*, 25(1), 69–80(2024). https://doi.org/10.21743/PJAEC/2024.06.07

Jayabal, R., Nanomaterials in Regenerative Medicine: Advancing the Future of Tissue Engineering, *Regenerat. Eng. Translat. Med.*, (2025). https://doi.org/10.1007/s40883-025-00416-x

Jothinathan, D. B. and Suseem S, R., Plant-derived zinc oxide nanoparticles using Phaseolus vulgaris: Characterization and in vitro bioactivity evaluation, *Inorg. Chem. Commun.*, 183, 115799(2026). https://doi.org/10.1016/j.inoche.2025.115799

Kareem, M. M. and Vijaya Lakshmi, G., Antioxidant and Catalytic Activity of Biosynthesized NiO Nanoparticles using *Terminalia chebula* Fruit Extract, *Asian J. Chem.*, 34(1), 35–41(2022). https://doi.org/10.14233/ajchem.2022.23406

Kothandaraman, L., Navin Kumar, N. K., Palaniyappan, S., Dalaq, A. S. and Bodaghi, M., Material extrusion techniques for biomedical applications: Biomaterials and their performance – A review, *Mater. Today Commun.*, 49, 113707(2025). https://doi.org/10.1016/j.mtcomm.2025.113707

Kumar, M. S., Sailatha, S. and Gunasekaran, G., Eco-Friendly Synthesis, Characterization and Biological Activities of Silver Nanoparticles from *Terminalia chebula* Fruit, *Asian J. Chem.*, 37(5), 1229–1236(2025). https://doi.org/10.14233/ajchem.2025.33465

Kyana, J., Botha, R. S., Lufua, B. B., Lotanga, C. O., Malutshi, E. O., Mundeke, A. L., Eyobi, V. M., Kambale, E. K., Nuapia, Y. B., Balčiūnaitiene, A. and Memvanga, P. B., Combined anti-inflammatory and laxative effect of mango kernels-based effervescent suppositories loaded with (multi)metallic nanoparticles synthesized using ash of plantain peels and gel of *Aloe vera*, *Drug Delivery Translat. Res.*, (2025). https://doi.org/10.1007/s13346-025-01959-w

Lavanya, B., Aparna, Y. and Ramana, M. V., Synthesis, characterization of zinc oxide nanoparticles using *Terminalia mantaly* leaf extract and their antibacterial activity, *Mater. Today: Proce.*, 92, 1011–1016(2023). https://doi.org/10.1016/j.matpr.2023.05.001

Mahendran, M., Sivakavinesan, M., Subbabhat, S., Rajeshkumar, S., Annadurai, G. and Selvankumar, T., Biomedical Applications of *Moringa oleifera* Leaf Extract-Mediated Synthesized Silver Nanoparticles, *Int. J. Adv. Sci. Eng.*, 12(1), 5151–5161(2025). https://doi.org/10.29294/IJASE.12.1.2025.5151-5161

Miastkowska, M., Kulawik-Pióro, A. and Szczurek, M., Nanoemulsion gel formulation optimization for burn wounds: Analysis of rheological and sensory properties, *Process.*, 8(11), 1416(2020). https://doi.org/10.3390/pr8111416

Mohammadzadeh, M., Zarei, M., Abbasi, H., Webster, T. J. and Beheshtizadeh, N., Promoting osteogenesis and bone regeneration employing icariin-loaded nanoplatforms, *J. Bio. Eng.*, 18(1), 29(2024). https://doi.org/10.1186/s13036-024-00425-4

Mohanasundaram, P. and Mary, S. M., Binding properties and biological applications of green synthesized ZnO nanoparticles from neem flower, *Sci. Rep.*, 15(1) (2025). https://doi.org/10.1038/s41598-025-02157-x

Moulana, K. M., Hari, B. M. and Vijaya, L. G., Anticancer, antibacterial, antioxidant, and photo-catalytic activities of eco-friendly synthesized Ni nanoparticles, *Inorg. Chem. Commun.*, 148, 110274(2023). https://doi.org/10.1016/j.inoche.2022.110274

Suguna, S., Edison, T. N. J. I., Atchudan, R., Sundramoorthy, A. K. and Lee, Y. R., Green-Routed Carbon Dot-Adorned Silver Nanoparticles for the Catalytic Degradation of Organic Dyes, *Catal.*, 12(9), 937 (2022). https://doi.org/10.3390/catal12090937

Suresh, U., Panneerselvam, C., Aziz, A. T., Srinivasan, M. K., Hassan, M. M., Alasmari, A. and Mohammedsaleh, Z. M., Synthesis, characterisation and evaluation of polyethylene glycol–β-cyclodextrin–curcumin–zinc oxide nanoparticles for mosquitocidal, antibacterial and anticancer applications, *Sci. Rep.*, 16(1), (2026). https://doi.org/10.1038/s41598-025-32059-x

Thanikodi, S. and Jothi, A. S., Green Synthesis and Process Optimization of Zinc Oxide Nanoparticles Using Pseudomonas fluorescens: Taguchi–ANN-Based Evaluation of Physico-Chemical Parameters, *Turkish J. Eng.*, 10(1), 204–212(2026). https://doi.org/10.31127/tuje.1804146

Thanjavur, N., Buddolla, B. A., Bugude, L., Theyagarajan, K. and Kim, Y. J., Bio-capped ZnO nanoparticles formulated from Prosopis juliflora gum: Phytochemical characterization and therapeutic potential, *Int. J. Bio. Macromol.*, 334, 149092(2025). https://doi.org/10.1016/j.ijbiomac.2025.149092

Tharani, M., Rajeshkumar, S., Al-Ghanim, K. A., Nicoletti, M., Sachivkina, N. and Govindarajan, M., *Terminalia chebula*-Assisted Silver Nanoparticles: Biological Potential, Synthesis, Characterization, and Ecotoxicity, *Biomed.*, 11(5), 1472(2023). https://doi.org/10.3390/biomedicines11051472

Wani, S. and Thirumalini, T., Influence of age of fermented *Terminalia chebula* fruit extract in shell lime: An ancient lime putty production technique adopted in Indian heritage structures, *J. Build. Eng.*, 98, 111054(2024). https://doi.org/10.1016/j.jobe.2024.111054